## **OPEN ACCESS**



# 3D Spectroscopy with GTC-MEGARA of the Triple AGN Candidate in SDSS J102700.40 +174900.8

Erika Benítez<sup>1</sup>, Héctor Ibarra-Medel<sup>1,2</sup>, Castalia Alenka Negrete<sup>3</sup>, Irene Cruz-González<sup>1</sup>, José Miguel Rodríguez-Espinosa<sup>4,5</sup>, Xin Liu<sup>6,7</sup>, and Yue Shen<sup>6,7</sup>, 10 

<sup>1</sup> Universidad Nacional Autónoma de México, Instituto de Astronomía, AP 70-264, CDMX 04510, Mexico; erika@astro.unam.mx

<sup>2</sup> Escuela Superior de Física y Matemáticas, Instituto Politécnico Nacional, U.P. Adolfo López Mateos, C.P. 07738, Ciudad de México, México

<sup>3</sup> Conacyt Research Fellow at Universidad Nacional Autónoma de México, Instituto de Astronomía, AP 70-264, CDMX 04510, Mexico

<sup>4</sup> Instituto de Astrofísica de Canarias, Vía Láctea, s/n, E-38205, La Laguna, Spain

<sup>5</sup> Departamento de Astrofísica, Universidad de La Laguna (ULL), E-38205, Spain

<sup>6</sup> Department of Astronomy, University of Illinois at Urbana-Champaign, Urbana, IL 61801, USA

National Center for Supercomputing Applications, University of Illinois at Urbana-Champaign, Urbana, IL 61801, USA

\*\*Received 2023 March 6; revised 2023 April 17; accepted 2023 April 17; published 2023 July 17

#### **Abstract**

Triple–active galactic nucleus (AGN) systems are expected to be the result of the hierarchical model of galaxy formation. Since there are very few of them confirmed as such, we present the results of a new study of the triple AGN candidate SDSS J102700.40+174900.8 (center nucleus) through observations with the GTC-MEGARA Integral Field Unit. 1D and 2D analysis of the line ratios of the three nuclei allow us to locate them in the EW(H $\alpha$ ) versus [N II]/H $\alpha$  diagram. The central nucleus is found to be a retired galaxy (or fake AGN). The neighbors are found to be a strong AGN (southeastern nucleus, J102700.55+174900.2), compatible with a Seyfert 2 (Sy2) galaxy, and a weak AGN (northern nucleus, J102700.38+174902.6), compatible with a LINER2. We find evidence that the neighbors constitute a dual AGN system (Sy2–LINER2) with a projected separation of 3.98 kpc in the optical bands. The H $\alpha$  velocity map shows that the northern nucleus has an H $\alpha$  emission with a velocity offset of  $\sim$ -500 km s<sup>-1</sup>, whereas the southeastern nucleus has a rotating disk and H $\alpha$  extended emission at kiloparsec scales. Chandra archival data confirm that the neighbors have X-ray (0.5–2) keV and (2–7) keV emission, whereas the center nucleus shows no X-ray emission. A collisional ring with knots is observed in Hubble Space Telescope images of the southeastern nucleus. These knots coincide with star formation regions that, along with the ring, are predicted in a head-on collision. In this case, the morphology changes are probably due to a minor merger that was produced by the passing of the northern through the southeastern nucleus.

*Unified Astronomy Thesaurus concepts*: Active galactic nuclei (16); Astronomical techniques (1684); Galaxy interactions (600); Seyfert galaxies (1447); Galaxy spectroscopy (2171); X-ray active galactic nuclei (2035)

#### 1. Introduction

Galaxy mergers are major events that play an important role in galaxy evolution within the hierarchical Lambda cold dark matter (White & Rees 1978; White & Frenk 1991; Springel et al. 2005) cosmology. They are found to be involved in the triggering of bursts of star formation (SF; e.g., Barnes & Hernquist 1991, 1996; Barnes 2004; Chien & Barnes 2010; Hopkins et al. 2013; Blumenthal & Barnes 2018) and in the accretion of material onto a central supermassive black hole (SMBH; Di Matteo et al. 2005; Hopkins et al. 2006; Di Matteo et al. 2008; Hopkins et al. 2008).

Since it is well established that almost all massive galaxies harbor a central SMBH (Kormendy & Richstone 1995; Magorrian et al. 1998; Ferrarese & Merritt 2000; Gebhardt et al. 2000), then galaxy interactions can involve two or more SMBHs getting closer before the final coalescence phase.

Dual active galactic nuclei (DAGNs) are thus expected to be found in the framework of galaxy hierarchical evolutionary models. DAGNs harbor two active SMBHs and simulations show that they are systems in an intermediate evolutionary stage between the first encounter and final coalescence of two

Original content from this work may be used under the terms of the Creative Commons Attribution 4.0 licence. Any further distribution of this work must maintain attribution to the author(s) and the title of the work, journal citation and DOI.

merging gas-rich galaxies (see De Rosa et al. 2019 for a review). In this evolutionary phase, the two SMBHs show a spatial projected separation of  $1-100\,\mathrm{kpc}$ . This phase can last  $\sim\!100\,\mathrm{million}$  yr (see Capelo et al. 2017), and during this time both SMBHs show AGN activity (Van Wassenhove et al. 2012; Blecha et al. 2013, 2018).

DAGNs are hard to detect, mainly due to their small (sometimes <1") spatial projected separations. So, multi-wavelength studies, particularly observations in the radio and X-ray bands, are ideal for confirming them as such (see, e.g., Benítez et al. 2019, 2022). In the optical bands, DAGNs candidates can be selected using data from surveys like the Sloan Digital Sky Survey (SDSS). Images showing two or more nuclei and with double-peaked narrow emission lines in their spectra (Wang et al. 2009; Liu et al. 2010; Smith et al. 2010; Ge et al. 2012; Kim et al. 2020) can be related to a pair of SMBHs that have kiloparsec-scale projected separations with overlapping emission from their narrow line region. We will refer to double-peaked narrow emission line AGNs as DPAGNs.

Triple AGNs can also form during the merger process if, for example, DAGNs merges with another AGN in its way, and the three are simultaneously accreting. However, there are very few triple-AGN systems confirmed up to now (Pfeifle et al. 2019; Yadav et al. 2021). Determining the rates of DAGNs or multiple AGNs in galaxy mergers will require exploring

merger-induced activity in AGNs and SMBH growth and evolution.

SDSS J102700.40+174900.8 (hereafter, we will refer to it as J102700.40+174900.8) is classified as a galaxy in SDSS Data Release 7 (DR7; Abazajian et al. 2009) with a redshift z = 0.066. J102700.40+174900.8 visually shows in the optical bands that it is part of three intense and apparently nearby nuclear sources. In a previous work by Liu et al. (2011; hereafter, L11), they show that it is a system of three emission line nuclei, two of which are offset by 450 and 110 km s<sup>-1</sup> in velocity and by 2.4 and 3.0 kpc in projected separation from the central nucleus (i.e., from J102700.40+174900.8). Therefore, the authors present evidence of a kiloparsec-scale triple-AGN system. Also, they have found that the three nuclei are obscured AGN, based on optical diagnostic emission line ratios, and obtained estimates of their BH masses using the  $M_{\rm BH}$ - $\sigma_{\star}$  correlation given in Tremaine et al. (2002). Based on the Baldwin, Peterson, Terlevich (BPT) diagnostic diagrams (see Baldwin et al. 1981; Veilleux & Osterbrock 1987), L11 find that source J102700.40+174900.8 (identified as "A" in their Figure 1) is in the locus of the low-ionization narrow emission region, i.e., it is a LINER source (Heckman 1980). In the case of J102700.55 +174900.2 (source B, to the southeast of A), it is found in the locus between the AGN and HII regions, and for source J102700.38+174902.6 (source C, to the north of A), it appears in the locus between Seyfert and LINER galaxies.

In this work, we present an optical and kinematical study of the triple AGN candidate J102700.40+174900.8, through observations carried out with the Gran Telescopio Canarias (GTC) and the Multi-Espectrógrafo de Alta Resolución para Astronomía (MEGARA) instrument. With MEGARA, we apply the Integral Field Spectroscopy (IFS) observational technique, which can spatially resolve the spectral information of an object with the instrumental implementation of the Integral Field Units (IFUs; see Sánchez 2020 for a review). Therefore, with IFS data, it is possible to spectroscopically disentangle the associated sources to J102700.40+174900.8. We also present an analysis of high-resolution *U*- and *Y*-band imaging from the Hubble Space Telescope<sup>9</sup> (HST), data from the Legacy SDSS survey (York et al. 2000), and archival data of the Chandra X-ray space telescope. In Section 2, the observations and data processing are presented. The data analysis appears in Section 3. Results and discussion are given in Section 4 and Section 5. Finally, conclusions are presented in Section 6. The cosmology adopted in this work is  $H_0 = 69.6 \, \mathrm{km \, s^{-1} \, Mpc^{-1}}$ ,  $\Omega_m = 0.286$ , and  $\Omega_{\lambda} = 0.714$  (Bennett et al. 2014).

#### 2. Observations and Data Processing

# 2.1. MEGARA

The instrument MEGARA is located in the Cassegrain focus of the GTC (see Carrasco et al. 2018). We used the IFU mode of MEGARA, also called the Large Compact Bundle, which provides a field of view (FOV) of  $12.5 \times 11.3$ . Observations were done in GTC3-21AMEX and GTC8-21BMEX (PI: Benítez) in order to cover the blue and red spectral ranges. The three nuclei in J102700.40+174900.8 (see the left panel of

Figure 1 and Table 1) were observed. In all blocks, the position of the telescope was centered at J102700.40+174900.8. This position guaranteed that the three nuclei were inside the FOV of MEGARA. Details of the observations are shown in Table 2.

#### 2.2. Processing the Data Cubes

## 2.2.1. 2D Reduction

We use the MEGARA official Data Reduction Pipeline (MEGARA DRP)<sup>10</sup> to perform the data reduction. MEGARA DRP performs the standard reduction of the raw multifiber exposures: bias subtraction, fiber extraction, fiber flat-field correction, flexure correction, wavelength calibration, and flux calibration. For the flux calibration, we use the spectrophotometry standard stars HR5501 and HR1544 from the Oke (1990) and Hamuy et al. (1992) catalogs. The final output for the MEGARA DRP is a fits file that contains the science-calibrated row-stack spectra (RSS) for each fiber, with metadata that have the relative fiber positions to the IFU center. In addition, we correct our wavelength solution to have a radial velocity in the heliocentric reference frame.

#### 2.2.2. 3D Reduction

With the flux- and wavelength-calibrated RSS, we proceed to rearrange and reconstruct the final data cube with a homogeneous spatial grid sampling. To create the spatially resampled data cube, we apply the methodology described in Ibarra-Medel et al. (2019), which is based on the same methodology used in the MaNGA (Law et al. 2016) and CALIFA (Sánchez et al. 2012) surveys. The method interpolates the flux at each spaxel of a given spatial grid using the next expression:

$$F_{x,y}(\lambda) = \sum_{i}^{n_{\text{fib}}} w(\lambda, r_i) F_i(\lambda) / \sum_{i}^{n_{\text{fib}}} w(\lambda, r_i), \tag{1}$$

where the value of  $F_i(\lambda)$  is the 1D spectra from the *i*th fiber from the calibrated RSS. The weight  $w(\lambda, r)$  is a Gaussian kernel defined as  $w(\lambda, r) = \exp(-0.5(r_{\lambda}/\sigma)^2)$ , with r as the distance from the spaxel (x, y) to the center of the fiber i at wavelength  $\lambda$ . We set a value of  $\sigma = 0.131$ , to obtain a weighting kernel with an FWHM comparable with the diameter size of the MEGARA fiber size (0.162). Finally, we define the final spaxel scale to be 0.135 spaxel<sup>-1</sup>, to avoid any spatial oversampling when considering the fiber diameter size.

# 2.2.3. Atmospheric Differential Refraction

We consider the wavelength dependency of the atmospheric differential refraction (ADR) on the cube reconstruction. To implement a correction of the ADR, we first use the international atomic time (TAI) of each exposure to estimate the effective TAI for the total OB. Then, we use the exact position of the GTC observatory to estimate the effective zenith angle (z) of the OB. Hence, we calculate the ADR shift with the use of the Filippenko (1982) formulation, based on the

 $<sup>\</sup>frac{8}{8}$  At z = 0.066, the spatial scale of 1" corresponds to 1.274 kpc (Wright 2006).

<sup>&</sup>lt;sup>9</sup> All the HST data used in this paper can be found in MAST: doi:10.17909/bkz9-zr94.

https://megaradrp.readthedocs.io/en/stable/

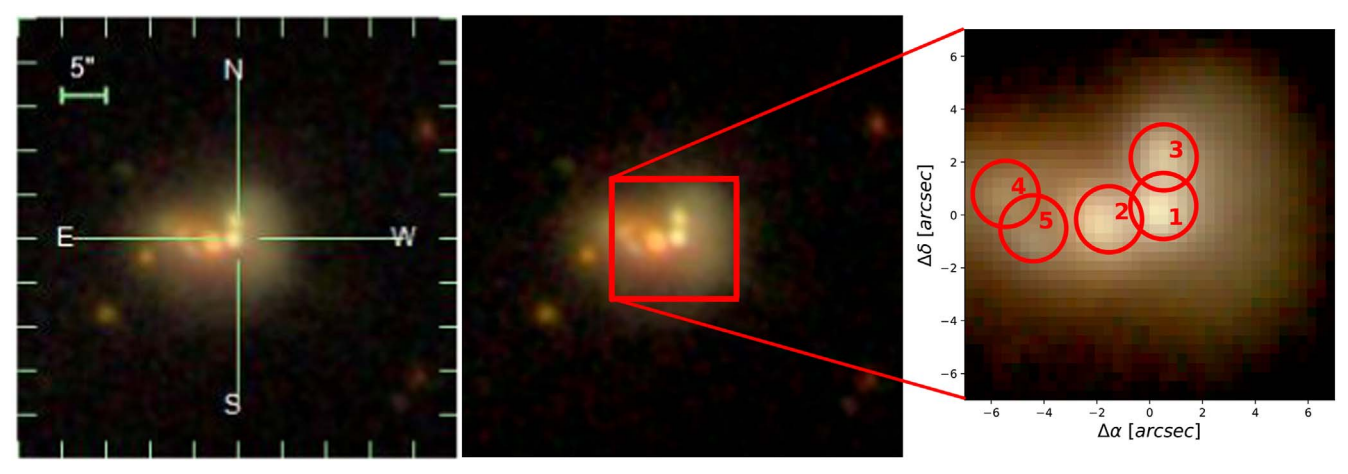


**Figure 1.** Left panel: SDSS DR7 image centered at J102700.40+174900.8, obtained at MJD 53710 (2005 December 6). The image shows the three nuclear sources: one at the center coordinates of J102700.40+174900.8 and two more, one to the north and the other to the southeast. See Table 1 for target identifications. Central panel: the same as in the left image, but showing in a red box the MEGARA FOV. Right panel: the reconstructed rgb image from the MEGARA IFU cube. The red circles show the five selected regions that were analyzed in this work, all of them with an aperture of 2.15.

Table 1
Target Identification

Target (1)	L11 (2)	This Work (3)
SDSS J102700.40+174900.8	A	1
SDSS J102700.55+174900.2	В	2
SDSS J102700.38+174902.6	C	3

**Note.** The three principal nuclei are identified with the nomenclature previously used by L11 and, for simplicity, in the images shown in this work.

Smart (1931) formula:

$$\Delta R(\lambda, \lambda_0, z, T, P, f)$$
= 180 × 3600  $\frac{R(\lambda, T, P, f) - R(\lambda_0, T, P, f)}{10^6 \pi} \tan z$ ,
$$R(\lambda, T, P, f) = (n(\lambda)_{T, P, f} - 1) \times 10^6.$$
 (2)

The value of n is the refraction index of the air as a function of the wavelength. The parameters T, P, and f indicate the dependency of the air temperature, atmospheric pressure, and water vapor pressure of the observational site (Filippenko 1982).  $\Delta R(\lambda, \lambda_0, z, T, P, f)$  is the shift (in arcseconds) of the target at a specific wavelength in reference to the wavelength  $\lambda_0$ . The shift direction in reference to the north celestial pole is given by the parallactic angle. Therefore, we can accurately measure the spatial shift per wavelength in reference to the center position of the IFU, and correct this shift in Equation (1) for all wavelength sampling. The air temperature, atmospheric pressure, and water vapor pressure are taken from the observational log information and from the headers of the fits raw exposures.

## 2.2.4. VPH Coadding

In this step, we obtain four data cubes, one per volume phase holographic (VPH)/OB. We proceed to coadd the four data cubes in one single data cube that has a spectral coverage from 4340 Å to 7303 Å. To do so, we use the surface brightness distribution of the three nuclei to estimate their central positions per each observing block (OB) within the data cubes. We estimate the shifts between the three centroids of the OB with VPH675 and between the centroids of the remaining OBs. With these shifts, we can calculate

a 2D transformation to spatially shift and rotate the VPH570, VPH521, and VPH480 data cubes to be exactly at the same spatial position within the FOV of the data cube of VPH675. In this step, we implement a 2D surface interpolation of the spatial grid per each spectral sampling. The interpolation generates a new set of data cubes for VPH570, VPH521, and VPH480, with the same spatial grid and FOV of the VPH675 data cube. Then, we define a new data cube with the total spectral range of the combined VPHs (4340 Å-7303 Å). In this case, we set the spectral sampling to 0.25 Å per pixel, and we degrade the spectral resolution for all the data cubes to R = 5000 (VPH 480), which is the lowest resolution of the four VPHs. To degrade the spectral resolution, we convolve the spectra with a Gaussian filter that has an FWHM defined as  $\Delta\lambda^2 = \Delta\lambda_{5000}^2 - \Delta\lambda_0^2$ , with  $\Delta\lambda_{5000}$  being the spectral resolution of VPH 480 and  $\Delta\lambda_0$  being the original spectral resolution of the degraded spectra. Finally, we interpolate the spectra of each data cube within the new spectral sampling. In the spectral regions where two or more VPHs overlap, we obtain the average flux among them. Therefore, we obtain a single data cube that merges the four OBs.

## 2.2.5. The Noise Spectrum

To estimate the noise spectrum of the final cube, we smooth the resolved spectrum spaxel by spaxel with a Gaussian kernel of  $\sigma = 100 \,\text{Å}$ , in order to damp the contribution of the strong emission lines and to obtain a smooth spectrum that traces the continuum. With the smoothed spectrum, we obtain a residual spectrum, defined as the original minus the smoothed spectrum. With the residual spectrum, we calculate the  $1\sigma$  percentile (25th-75th percentile) values of the spectral residuals within a shifting window of 800 Å. This window is centered at each spectral sampling of the spectrum; therefore, we obtain the  $1\sigma$ percentile of the residuals at each wavelength. The use of the  $1\sigma$  percentile rejects the outliers associated with the emission lines and gives the effective variance associated with the observed spectra. In Figure 2, we show an example of the final signal-to-noise ratio (S/N) of the spectra within our reduced data cube. We recuperate an average S/N of ≈60 in the VPH675 spectral region. This VPH has the largest exposure time for our observational campaign. The lowest S/N corresponds to VPH480, with an average S/N of  $\approx 7$ . Unfortunately, the VPH480 spectral region that was selected

Table 2
Log of Observations

Date Obs	VPH	R	Spectral Range	Exposure Time	Moon	Sky	Airmass	Seeing
			Å	S			"	
(1)	(2)	(3)	(4)	(5)	(6)	(7)	(8)	(9)
2021 Mar 2	675LR-R	5900	6096.54-7303.21	1860	Gray	Clear	1.2	0.6
2022 Jan 1	570LR-V	5850	5143.74-6168.19	1116	Dark	Clear	1.5	1
2022 Mar 4	521MR-G	12000	4963.22-5445	900	Dark	Clear	1.1	1.1
2022 Mar 5	480LR-B	5000	4332.05-5199.96	900	Dark	Clear	1.1	1.1

to observe the  $H\beta$  complex is obscured by dust, and the S/N in this spectral region is not enough to achieve a good detection.

## 2.2.6. Astrometry

With the merged data cube, we now proceed to calculate accurate astrometry. We use the SDSS r-band photometric image of the region of J102700.40+174900.8. We calculate the centroids of the three nuclei within the SDSS photometric image and compare them with the centroids of the same three nuclei within the FOV of the data cube. With this information, we obtain the World Coordinate System (WCS) for the merged data cube to match the WCS of the r-band SDSS photometric image. The astrometric positions and redshifts of the five selected regions are shown in Table 3 and the projected separations between the three nuclei are given in Table 4.

#### 2.2.7. Second-order Spectrophotometric Correction

We use the SDSS g and r photometric bands to create a second-order correction on the spectrophotometry calibration. The SDSS r band and most of the g band fit within the merged data cube spectral range of 4340 Å–7303 Å. Therefore, we can calculate the synthetic r- and g-band photometric fluxes from the data cube. With the synthetic fluxes, we measure any flux deviation from the SDSS photometry and calculate a 2D flux correction for our data cube to reproduce the SDSS g-r colors. Finally, we correct the final data cube by the galactic extinction, using the Schlafly & Finkbeiner (2011) galactic dust extinction maps with the Fitzpatrick (1999) extinction law.

## 2.2.8. Point-spread Function Characterization

To characterize the effective point-spread function (PSF) within our final MEGARA data cube, we first apply the same reduction procedure (described above) to the standard star HR1544 to recuperate its data cube. The effective PSF on an IFU observation is the total contribution of the telescope seeing and the 2D reconstruction of the data cube (Ibarra-Medel et al. 2019; Sánchez 2020). With the data cube of HR1544, we perform a surface brightness  $(\mu)$  profile fitting, following the methodology described in H. Ibarra-Medel et al. (2023, in preparation) and in Ibarra-Medel (2022). The methodology first integrates the cube along the spectral axis to obtain a highresolution  $\mu$  map. Then, we perform the  $\mu$  profile fitting, with the use of a Moffat profile (Moffat 1969; Trujillo et al. 2001). For completeness, we also explore a Gaussian  $\mu$  profile. The  $\mu$ fitting uses a Markov Chain Monte Carlo (MCMC) method. We find that the effective PSF of our reconstructed data cube has a Moffat profile with an FWHM of 1."25 with a  $\beta$  value of 9.32. The  $\beta$  value indicates the extension of the PSF wings. When  $\beta$  asymptotically tends to infinite, the Moffat profile tends to a Gaussian shape. If we fit a Gaussian profile directly,

we obtain a PSF FWHM of 0."87. The difference between the Gaussian fit and the Moffat fit is due to the PSF tail contribution to the profile. Therefore, we use the Moffat fitting to characterize the effective PSF of our data cube. This gives us an effective spatial resolution of 1."25 within the cube.

#### 3. Data Analysis

## 3.1. Stellar Spectra Modeling

To model the stellar spectra, we use the PYPIPE3D<sup>11</sup> spectral fitting tool. For the stellar fitting, this tool uses the FIT3D pipeline, which performs a single stellar population (SSP) synthesis (Sánchez et al. 2016a, 2016b; Lacerda et al. 2022). The workflow of PYPIPE3D has been described in detail in several works (e.g., Ibarra-Medel 2022; Ibarra-Medel et al. 2022; Sánchez et al. 2022), but we can summarize it as follows. (a) It estimates the initial values of the redshift and kinematics from the central spectra. (b) It performs spatial segmentation to achieve a target S/N of 50. (c) It obtains for each spatial bin a first model of the stellar spectra. PYPIPE3D uses this model to obtain a gas spectrum, from which it models the strong emission lines. (d) PYPIPE3D subtracts the models of the strong emission lines from the original spectra and runs FIT3D using a full stellar library to obtain the final SSP synthesis. For this work, we use the gsd-156 stellar library defined in Cid Fernandes et al. (2013). This uses 156 SSP templates that cover 39 stellar ages (from 1 Myr to 14.2 Gyr), and four metallicities  $(Z/Z_{\odot} = 0.2, 0.4, 1, \text{ and } 1.5)$ . This library uses a Salpeter (1955) initial mass function (IMF). In addition, PYFIT3D considers a Cardelli et al. (1989) dust attenuation law for internal extinction. (e) Finally, PYPIPE3D saves the results of the stellar fitting and returns a set of 2D maps of the stellar properties. The maps contain the same number of spaxels as the original data cube.

In this study, we use the gas spectra calculated in step (c) to model and calculate our emission line analysis. We do not use the PYPIPE3D analysis because we implement a more complex emission line fitting that considers a double emission line deblending and a broad component. However, we use the PYPIPE3D stellar properties returned by the SSP analysis to obtain stellar velocity dispersion and stellar masses.

## 3.2. Single-aperture Line Profile Modeling

In this section, we present the emission line profile modeling obtained for the five regions within the MEGARA FOV. Since we are limited by the spatial resolution of the data cube, the five spectral regions were extracted with an aperture of 2"5, i.e., two times the PSF, as we have shown in Figure 1.

<sup>11</sup> https://gitlab.com/pipe3d/pyPipe3D/

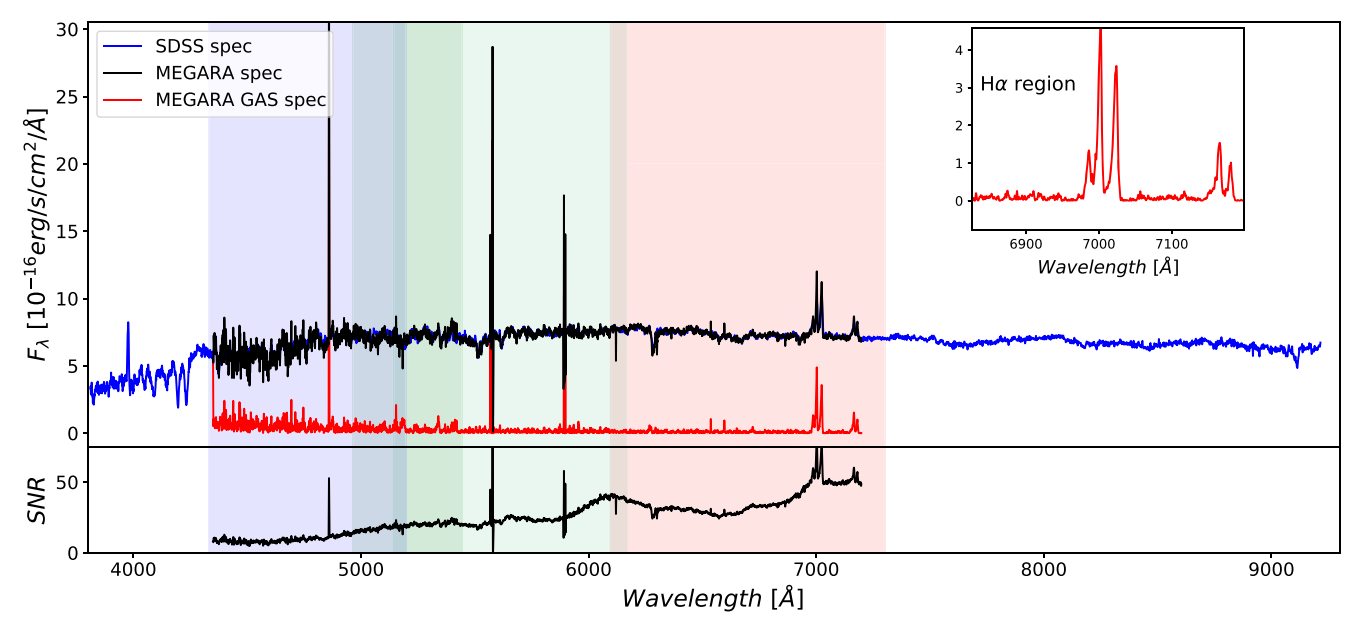


Figure 2. In the upper panel, we show in black the MEGARA spectrum extracted with a fiber aperture of 3'', centered in the fiber position of the SDSS archival spectrum of J102700.40+174900.8, obtained at MJD 54140 (2007 February 9). The archival SDSS spectrum appears overlapped in blue. In red, we show the gas spectrum obtained after subtracting the contribution from the stellar population, using PYPIPE3D. The shaded color regions represent the MEGARA VPH spectral regions: blue for VPH480 LR-B, dark green for VPH521 MR-G, light green for VPH570 LR-V, and red for VPH675 LR-R. The inset panel shows a zoom-in of the H $\alpha$  region for the gas spectrum. The lower panel shows the S/N of the MEGARA spectrum.

Table 3
Astrometric Positions

Region (1)	R.A. (2)	Decl. (3)	Aperture Radius (4)	z (5)
1	10:27:00.375	17:49:00.81	1.25	0.067
2	10:27:00.529	+17:49:00.57	1.25	0.066
3	10:27:00.358	+17:49:02.95	1.25	0.065
4	10:27:00.808	+17:49:01.41	1.25	0.066
5	10:27:00.717	+17:49:00.21	1.25	0.066

**Notes.** R.A. and decl. are (J2000). The aperture radius (in arcsec) is used to analyze the five selected regions of the MEGARA data.

Table 4
Region Separation

Regions	Distance	Distance kpc
(1)	(2)	kpc (3)
1–2	2.12	2.70
1–3	1.84	2.35
2–3	3.12	3.98

**Note.** The distances among the three principal nuclei are in arcsec and in kpc, with z=0.066.

The emission line profiles were modeled using the IRAF/specfit routine (Kriss 1994). This package allows us to model, at the same time, the underlying continuum and the emission lines. The line fitting was done using Gaussian profiles, for which specfit uses three input parameters: the central wavelength, the line intensity, and the FWHM. The best fit was found by minimizing the  $\chi^2$  using the Marquardt algorithm for 5–10 iterations. The fits were performed in three regions: 4850 Å–5050 Å for H $\beta$ , 6200 Å–6420 Å for [OI], and 6500 Å–6745 Å for H $\alpha$ . We considered a power law with a nearly flat slope for the continuum in all three regions.

We start with the line fitting in the  $H\alpha$  spectral regions because it has the most prominent lines. For all the regions, we modeled  $H\alpha$  and the doublets of the [N II] and [S II] $\lambda\lambda$  6716, 6731 narrow components, constraining the FWHM to be equal in all the lines. We assume that they originate in the same clouds and therefore share the same kinematics. The intensity of [N II] $\lambda$ 6548 was linked to [N II] $\lambda$ 6583, taking into account the theoretical 3:1 ratio. The lambda shift of this doublet was also linked to being the same. The residuals obtained in the fittings of regions 1 and 3 indicate that a second Gaussian component is needed to obtain the best fit (see Figure 3).

Therefore, for regions 1 and 3, the constraints on the FWHM were considered for each set of lines (blue- and redshifted components). J102700.55+174900.2 was instead modeled with a single Gaussian component.

The  $H\beta$  and [OI] spectral regions were fitted with the same components as their respective  $H\alpha$  regions, with the doublets of [OI] and [O III] fitted similarly to [N II]. Only in regions 1, 2, and 3 is [O III] visible. In regions 1 and 2, we can see hints of  $H\beta$  emission, for which we attempted to fit a Gaussian component with the same FWHM as [O III]. However, the S/N was not enough to achieve a good fit, so these lines were not analyzed. It is worth mentioning that in the MEGARA spectra of these three regions, the  $H\beta$  emission line is dominated by noise, due to the low exposure time of VPH480 (see the left panels of Figure 3). The line profile modeling results for regions 4 and 5 are shown in Figure 4. Both regions were fitted with single Gaussian components and are found to be SF regions. The FWHMs of the emission line profiles obtained for the five regions are presented in Table 6.

# 3.3. 2D Spatially Resolved Emission Line Profile Modeling

To exploit the full advantage of the IFS spatially resolved data, we implemented MCMC modeling of the [N II]6549, [N II]6585, and H $\alpha$  emission lines, spaxel by spaxel. In the

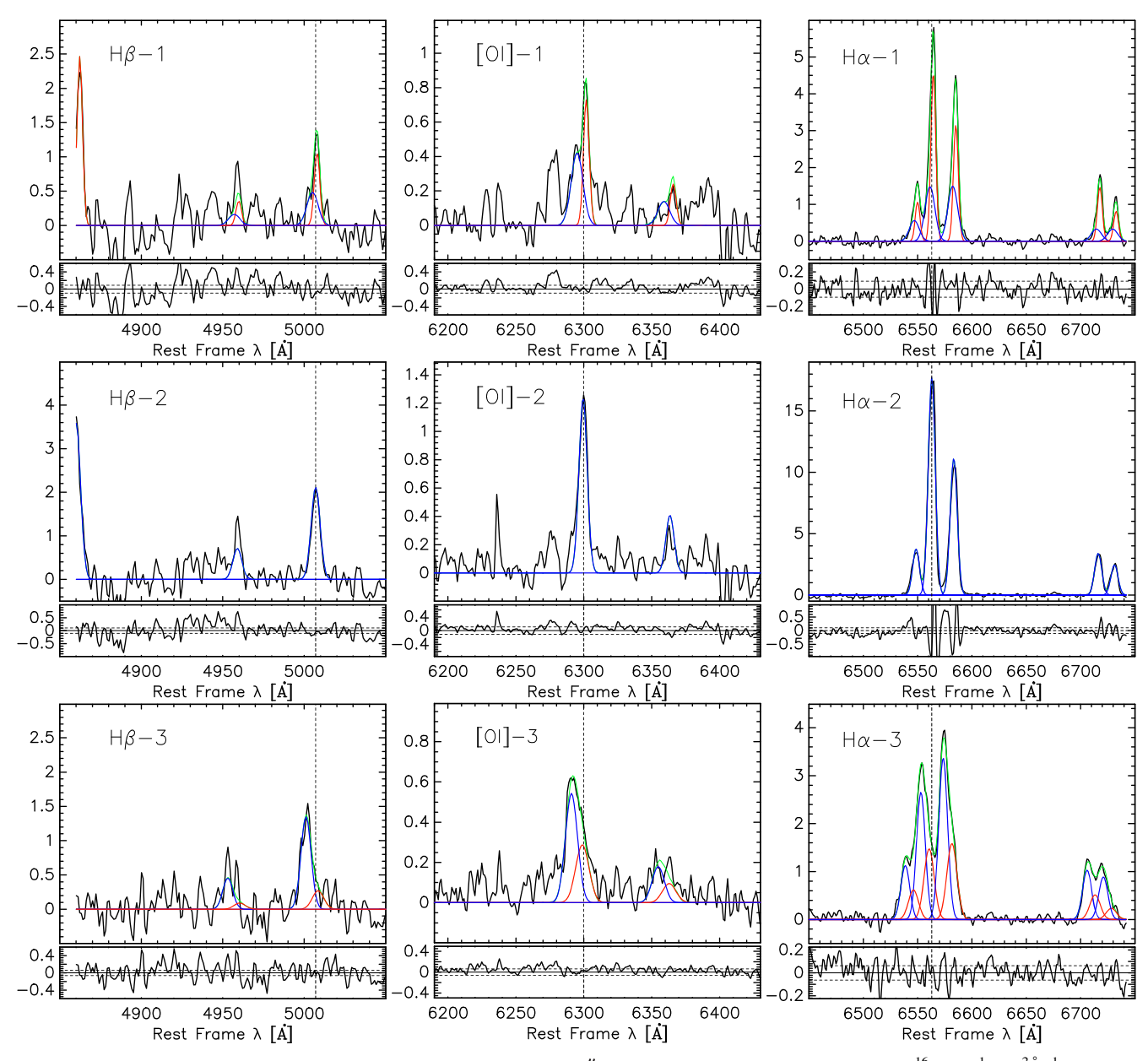


Figure 3. Line profile models for regions 1–3 with an aperture of 2."5. The vertical axis has flux units of  $\times$  10<sup>-16</sup> erg s<sup>-1</sup> cm<sup>-2</sup>Å<sup>-1</sup>.

previous section, we applied meticulous and detailed modeling of the strong emission lines for regions 1, 2, 3, 4, and 5. In this section, we apply a simplified fit that only considers one single narrow and broad component for the  $H\alpha$  region. We use the Foreman-Mackey et al. (2013) implementation of the Affine Invariant MCMC Ensemble Sampler with the use of the Python package EMCEE $^{12}$  to model the Hlpha region. The space parameters that we explore are the amplitudes of  $H\alpha$  and [N II]6585, the velocity shifts  $\Delta v_n$  of the narrow components, the FWHMs of the narrow components, the FWHM of the broad component, the velocity shift  $\Delta v_b$  of the broad component, and the amplitude of the broad component. The model fixes the relative velocity among H $\alpha$ , [N II]6549, and [NII]6585 with the values reported in Vanden Berk et al. (2001), and fixes the amplitude ratio of [N II]6585/[N II]6549 to 2.93. The velocity shift of the H $\alpha$  broad component is left

of the kinematic components of the narrow lines.

From the spatially resolved line profile fitting, we are able to obtain not only the velocity shifts of the narrow lines for our five regions, but also we are able to reconstruct the full line-of-sight (LOS) kinematic field of the narrow component within the MEGARA FOV. In Figure 6, we show the results of the spatially resolved kinematics. Here, we also do not find any evidence of the existence of a broad component in the three nuclei. The velocity map of the narrow components shows that part of the gas of J102700.38+174902.6 is blueshifted, with a maximum velocity of  $-500 \, \mathrm{km \, s^{-1}}$ . In the case of object

free. In Figure 5, we show an example of the MCMC

 $H\alpha$  region fitting in the central spaxel of our data cube. With

this analysis, we can reconstruct the 2D spatially resolved maps

<sup>4.</sup> Results
4.1. Velocity Maps

https://emcee.readthedocs.io/en/stable/

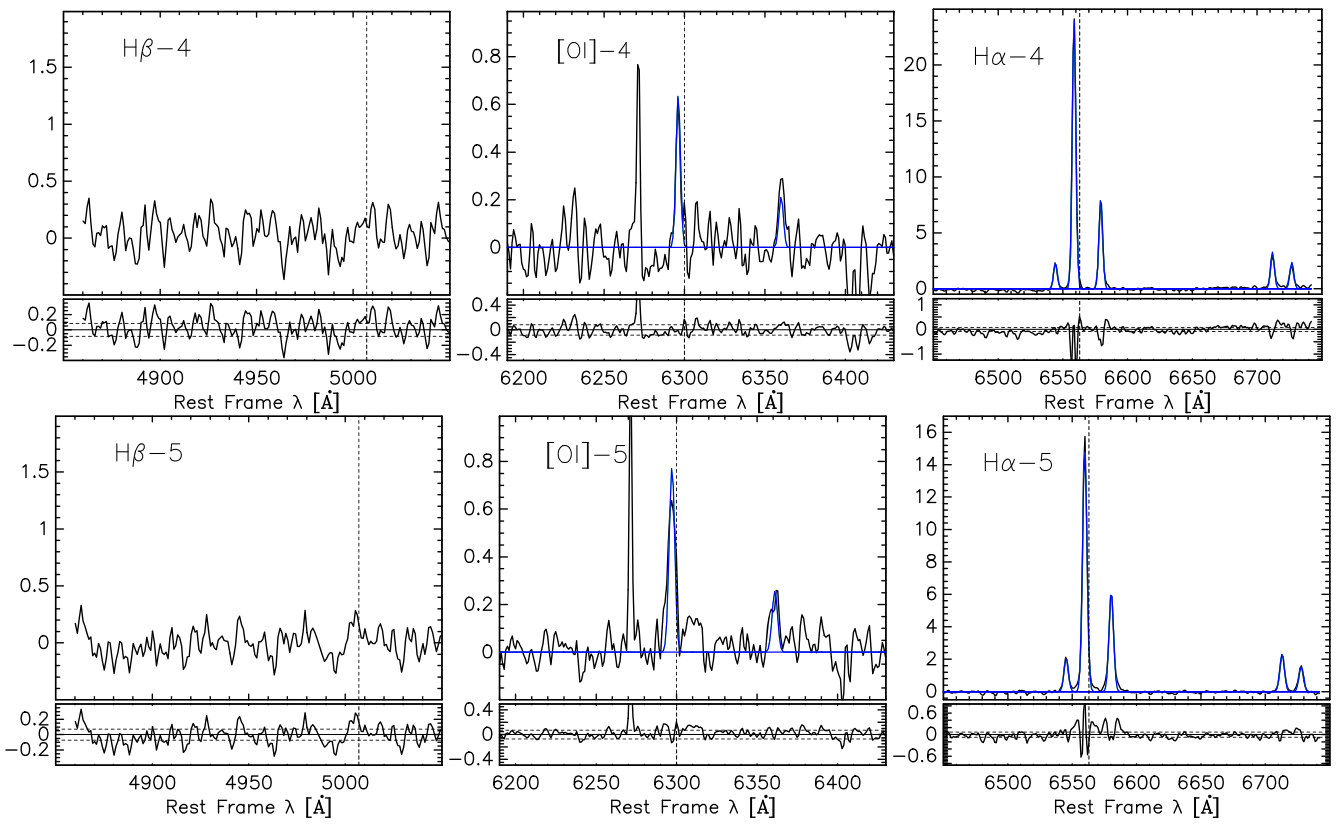


Figure 4. Line models for regions 4–5 with an aperture of 2".5. The vertical axis has flux units of  $\times 10^{-16}$  erg s<sup>-1</sup> cm<sup>-2</sup> Å<sup>-1</sup>.

J102700.55+174900.2, the isovelocity curves trace the rotation from a gaseous disk. In addition, the full velocity field shows the presence of an extended emission toward the southeast and west, up to  $\sim$ 6", which corresponds to  $\sim$ 7.6 kpc, and less extended toward the northeast,  $\sim$  4" or  $\sim$ 5.1 kpc.

#### 4.2. Velocity Shifts

Using the resolved velocity field, we explore the velocity profiles moving from J102700.55+174900.2 (region 2) to J102700.40+174900.8 (region 1), denoted as path 2-1 and a green arrow in Figure 6. We also explore the velocity profiles moving from object J102700.40+174900.8 (region 1) to J102700.38+174902.6 (region 3), path 1-3, marked with a red arrow in Figure 6. The velocity profile along path 1-3 clearly shows a blueshift of  $\approx -500 \,\mathrm{km \, s^{-1}}$  for object J102700.38 +174902.6with respect to J102700.40+174900.8 and J102700.55+174900.2. The velocity profile in 2-1 shows a velocity increment from zero (we set the velocity rest frame to the center of J102700.55+174900.2) to  $\approx$ 42 km s<sup>-1</sup> at the middle of the path, and then drops to  $-3 \,\mathrm{km \, s^{-1}}$ . This shape shows the velocity changes of the observed rotation of the gaseous disk in object J102700.55+174900.2 along path 2-1.

In addition, in the upper right panel of Figure 6, we show the actual line shifts along paths 1–3, 2–1, and A (the blue arrow in Figure 6) for H $\alpha$ , [N II] $\lambda$ 6548, and [N II] $\lambda$ 6583. The intensity map on that panel represents the total flux intensity of the lines in the spectral range 6530 Å–6600 Å along the paths. We also overplotted the rest-frame wavelengths of H $\alpha$ , [N II] $\lambda$ 6548, and [N II] $\lambda$ 6583, centered in J102700.40+174900.8, as a segmented blue line. For paths 1–3 (from region 1 to region 3), we observe how the emission lines start to have a blueshift at  $\approx$ 1″2 from the

center of J102700.40+174900.8. At  $\approx 1.^{\prime\prime}7$ , the emission lines reach their final shift ( $\approx -500 \text{ km s}^{-1}$ ). For paths 2–1, we observe a small shift, but we show that the principal emission line flux comes from region 2. And finally, in path A, we clearly observe how the emission lines have a shift from blue to red along path A, which is centered in region 2.

We now explore in more detail the shifts along path A, which traces the rotation of the gaseous disk in the object J102700.55 +174900.2. We measure the velocity change along path A (the blue arrow in Figure 6). Path A passes through the object J102700.55+174900.2 and it defines the path of the maximum velocity gradient: it passes perpendicularly through all isovelocity contours. The velocity profile along path A (lower right panel of Figure 6) shows a clear rotation curve that has a dynamical center within aperture 2, where J102700.55+174900.2 lies. It has a minimum velocity of  $-230\,\mathrm{km\,s^{-1}}$  and a maximum velocity of 140 km s<sup>-1</sup>. To characterize this rotation curve, we use the parameterization of Bertola et al. (1991) to obtain the value of  $V_{\rm max}$ , as discussed in Aquino-Ortíz et al. (2018). We show this parameterization as a black solid line in the lower right panel of Figure 6. We get a  $V_{\rm max}$  of 128.6  $\pm$  6 km s<sup>-1</sup>, with a systemic velocity of  $-57 \pm 3 \,\mathrm{km \, s}^{-1}$  and a rotation curve amplitude of  $185.6 \pm 6 \,\mathrm{km \, s^{-1}}$ 

## 4.3. Stellar Velocity Dispersion and Stellar Masses

Using the outputs of PYPIPE3D, we recover the SSP maps of the velocity dispersion  $(\sigma_{\star})$ , the total stellar flux, and the stellar mass within the FOV of MEGARA. To calculate the total velocity  $\sigma_{\star}$  within all apertures, we get the quadratic mean weighted by the stellar flux  $(F_{\rm ssp})$  of all the spaxels within each

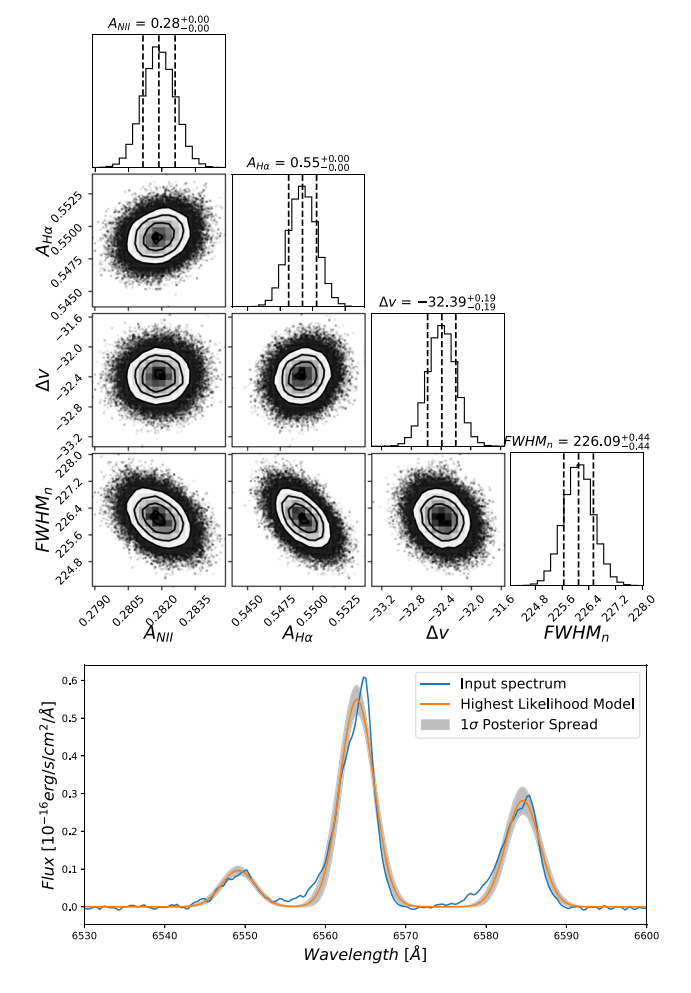


Figure 5. Example of a single-spaxel line-fitting model of  $H\alpha$  and [N II] using the MCMC method and a Gaussian profile. In the upper panel, we show the confidence plots of four of the seven free parameters of our fit: the amplitudes of  $H\alpha$  and [N II]6585, the velocity shifts  $\Delta v_n$  of the narrow components, and the FWHMs of the narrow components. We did not find the presence of a broad component. Lower panel: We plot the input spectra of the  $H\alpha$  region with the best-fit model; the shaded region shows the dispersion of our posterior line fit models within  $1\sigma$  confidence.

region, defined as:

$$\sigma_{\star} = \left(\frac{\sum_{i,j} \sigma_{\star,i,j}^2 \times F_{\text{ssp},i,j}}{\sum_{i,j} F_{\text{ssp},i,j}}\right)^{1/2},\tag{3}$$

where the indexes i, j are the indexes within the apertures of our regions. To obtain the total stellar mass, we simply get the total stellar mass contribution of all the spaxels within each region. We present the final values for the five regions in Table 6.

### 4.4. HST Images

We present the analysis of the high-resolution HST *U*- and *Y*-band imaging of the target obtained by Program GO 13112 (PI: Liu). Details of these observations are given in Table 5. For our study, we use the final reduced exposures taken with the Wide Field Camera 3 (WFC3) in the UV filter F336W (i.e., the *U* band) and in the IR filter F105W. In addition, the WFC3 (i.e., *Y*-band) instrument handbook<sup>13</sup> indicates that the FWHM PSF values are on the order of 0."13 for F105W and 0.08" for

F336W. Those exposures provide the necessary spatial resolution to resolve any substructure within our five regions.

The HST near-IR (NIR) image of J102700.40+174900.8 shows that regions 4 and 5, identified with MEGARA as SF regions, match in position with the knots found in the extended ring associated with J102700.55+174900.2; see Figure 7. The HST optical–UV image of J102700.40+174900.8 also confirms that J102700.55+174900.2 is disrupted, with a ring structure showing knots.

These images allow us to fit the best ellipse region that encloses at least the 50% of their total fluxes within their aperture regions (1.125 of radii). From these fittings, we measure object J102700.40+174900.8 (region 1) as having an elliptical shape with a semimiajor axis of 0.189 (1.13 kpc) and a semiminor axis of 0.172 (0.92 kpc). In the same way, object J102700.55+174900.2 (region 2) has a semimajor axis of 1.177 (2.26 kpc) with a semiminor axis of 0.176 (0.97 kpc), and object J102700.38+174902.6 (region 3) has a semimajor axis of 1.13 (1.144 kpc) with a semiminor axis of 0.158 (0.74 kpc).

## 4.5. Dynamic Mass

To calculate the dynamical mass for objects J102700.40 +174900.8, J102700.55+174900.2, and J102700.38 +174902.6 (regions 1, 2, and 3), we apply the virial theorem (Zwicky 1937) with the implementation of the  $S_K^2$  formulation (Weiner et al. 2006), defined as:

$$M_{\rm dyn} = \eta S_K^2 r_e G^{-1},\tag{4}$$

with  $S_K^2 = \sigma^2 + KV_{\rm rot}^2$ ,  $\sigma$  being the velocity dispersion,  $V_{\rm rot}$  being the rotation velocity, and  $r_e$  being the effective radius of the object. In this case, we follow the analysis of Aquino-Ortíz et al. (2018) and use the values of K=0.5 and  $\eta=1.8$  to estimate the total dynamical mass for our three regions. To estimate the value of  $r_e$ , we use our measurements of the semimajor axis of the three objects. In addition, we set the value of the gravitational constant G as  $4.3009 \times 10^{-6} \, {\rm kpc} \, M_\odot^{-1} \, ({\rm km \, s}^{-1})^2$ . We also use the estimations of  $\sigma_\star$  and  $V_{\rm max}$  to define  $\sigma$  and  $V_{\rm rot}$  for the  $S_K^2$  estimation. The final values of  $M_{\rm dyn}$ ,  $\sigma_\star$ , and  $V_{\rm max}$  are presented in Table 6.

#### 4.6. BH Mass Estimates

We estimate the BH mass of the three nuclei using the  $M_{\rm BH}$  versus  $\sigma_{\star}$  correlation of McConnell & Ma (2013):

$$\log_{10} \frac{M_{\rm BH}}{M_{\odot}} = 8.32 + 5.64 \log_{10} \left( \frac{\sigma_{\star}}{200 \,\mathrm{km \, s^{-1}}} \right). \tag{5}$$

We find that J102700.40+174900.8 hosts an SMBH with a mass of  $3.1 \times 10^9 M_{\odot}$ , while J102700.55+174900.2 has an SMBH mass of  $1.9 \times 10^9 M_{\odot}$  and J102700.38+174902.6 has an SMBH mass of  $1.7 \times 10^9 M_{\odot}$ .

# 4.7. WHAN Diagram

With the 2D spatially resolved emission lines of Section 3.3, we explore the resolved ionized emission properties along the MEGARA FOV. Hence, we obtain the map of the  $H\alpha$  equivalent width EW( $H\alpha$ ). We use the continuum flux within 6630 Å–6670 Å to obtain the value of EW( $H\alpha$ ). We show the continuum map (upper left panel) and the EW( $H\alpha$ ) (upper middle panel) in Figure 8. In addition, in the upper right panel of Figure 8, we obtain the map of the line ratio log [N II]/ $H\alpha$ .

<sup>&</sup>lt;sup>13</sup> From the HST user documentation: https://hst-docs.stsci.edu/wfc3ihb.

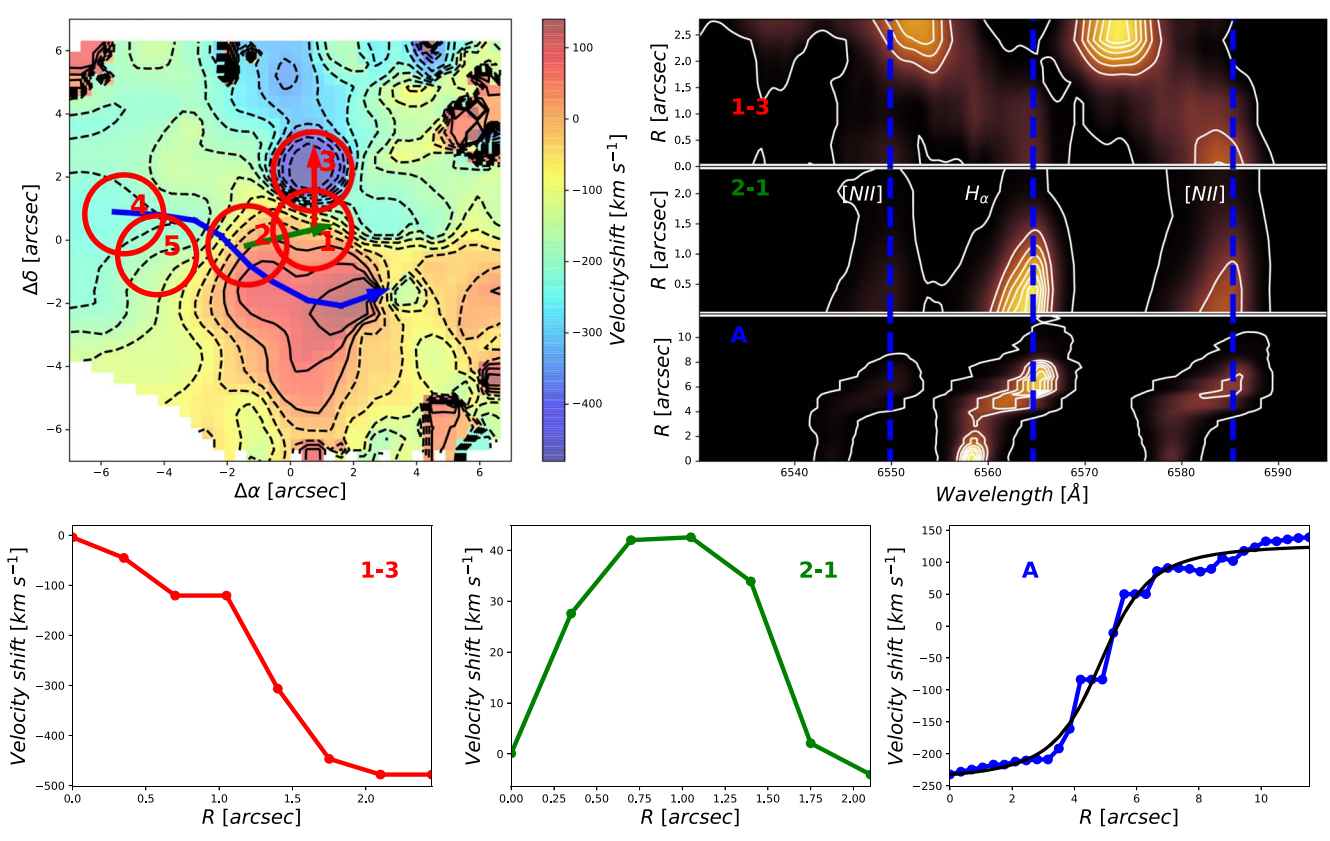


**Figure 6.** Upper left panel: velocity map of the narrow emission lines of  $H\alpha$ , with the paths 1–3 (red arrow), 2–1 (green arrow), and A (blue arrow) showing the paths of the explored velocity profiles. Upper right panel: 2D emission spectra of the  $H\alpha$  region within the segments 1–3, 2–1, and A. The dashed blue lines represent the wavelengths of the  $H\alpha$  and [N II] emission lines in the J102700.40+174900.8 (region 1) rest frame. Lower panels: velocity profiles along paths 1–3, 2–1, and A. For path A, the black solid line represents the best velocity profile fit using the Bertola et al. (1991) parameterization.

Table 5 HST Data

Filter	Exptime s	λ Å	FWHM PSF		
(1)	(2)	(3)	(4)		
F105W	238.704	10551.047	0.13		
F336W	2154.000	3354.656	0.08		

**Notes.** J102700.40+174900.8 HST data were obtained with WFC3 on 2013 March 27. The PSF values were obtained from the WFC3 HST user documentation.

In the EW(H\$\alpha\$) map, we find that in the locus of J102700.40 +174900.8, there is a depression of the EW(H\$\alpha\$) value with a minimum of \$\approx 2 \text{ Å}\$, while J102700.55+174900.2 has a larger value of 22 \text{ Å}\$, and J102700.38+174902.6 an intermediate value of 4 \text{ Å}\$. Furthermore, the EW(H\$\alpha\$) distribution shows the existence of an extended structure centered in J102700.55 +174900.2 that matches with the structure discussed in Section 4.4 and the disk velocity profile discussed in Section 4.2. Finally, in the locus of J102700.40+174900.8, we find a peak on the log [N II]/H\$\alpha\$ map, with a maximum value of 0.2 dex.

We now proceed to explore the EW(H $\alpha$ ) versus [N II]/H $\alpha$  diagram (WHAN; Cid Fernandes et al. 2011). In the lower left panel of Figure 8, we show the spatially resolved WHAN diagram. Following the definitions in Cid Fernandes et al. (2011), we separate the line ratios into four regions with the following color code. The light blue zones represent the regions with emission

within the SF region in the WHAN diagram: log [N II]/H $\alpha$  < 0.4 and EW(H $\alpha$ ) > 3 Å. The dark blue zones represent the regions with emissions that characterize a fake AGN: EW(H $\alpha$ ) < 3 Å. The yellow zones represent the regions within a weak-AGN region in the WHAN diagram: log [N II]/H $\alpha$  > -0.4 and 3 Å < EW(H $\alpha$ ) < 6 Å. The dark red zones represent the regions with strong-AGN emission: log [N II]/H $\alpha$  > -0.4 and EW(H $\alpha$ ) > 6 Å.

In addition, in the lower central panel of Figure 8, we estimate the positions in the WHAN diagram of the integrated values of our five regions. Hence, the spatially resolved and integrated WHAN diagrams show that J102700.40+174900.8 does not have any evidence of ionized gas emission that can be associated with an AGN or SF activity. The line ratios and EW(H $\alpha$ ) values indicate that J102700.40+174900.8 can be classified as a fake AGN or as a "retired galaxy" (RG; Cid Fernandes et al. 2011). The observed extended emission is associated with J102700.55+174900.2. This object shows the characteristic emission of a strong-AGN emission (Seyfert, according to Cid Fernandes et al. 2011). Meanwhile, J102700.38+174902.6 shows evidence of being a weak AGN in this diagram. For regions 4 and 5, we find the typical emission of SF regions. This conclusion is also corroborated in Section 4.4, identifying those regions as SF regions.

## 4.8. The DPAGN in J102700.40+174900.8

In Section 3.2, the detailed modeling of the emission line profiles of the five apertures shows that only J102700.40 +174900.8 (region 1) and J102700.38+174902.6 (region 3) have evidence of double-peaked narrow emission line components. This result would in principle suggest that both are DPAGNs.

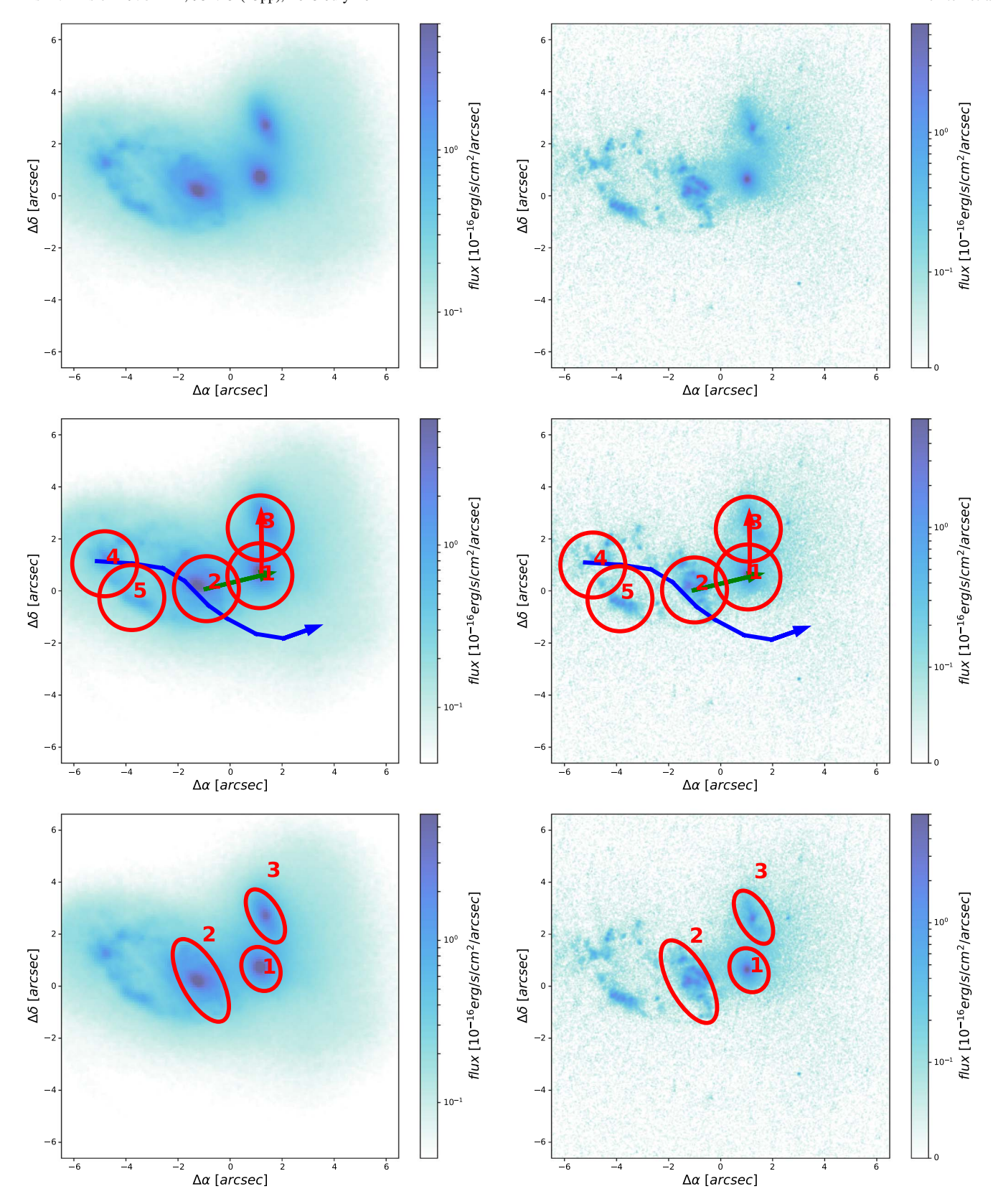


**Figure 7.** Left panels: the HST *Y*-band image of J102700.40+174900.8 within the FOV of MEGARA. Right panels: the HST *U*-band image of J102700.40 +174900.8 within the FOV of MEGARA. The upper panels show the HST images without any overplotted regions. The middle panels show the HST images with regions 1 to 5, and also the plots of paths 1–3 (red arrow), 2–1 (green arrow), and A (blue arrow) of Figure 6. The lower panels show the best-fit ellipse regions that contain at least 50% of the flux of regions 1, 2, and 3.

Table 6
Main Results

Region (1)	$FWHM_B  km s-1  (2)$	$FWHM_R  km s^{-1}  (3)$	$\stackrel{\mathrm{EW}_B}{\mathring{\mathrm{A}}}$	EW <sub>R</sub> Å (5)	$M_{\rm BH} = 10^9 M_{\odot}$ (6)	$M_{\star} \ 10^{10} M_{\odot} \ (7)$	$M_{\rm dyn} \ 10^{10} M_{\odot} \ (8)$	$\sigma_{\star}$ $\text{km s}^{-1}$ (9)	$V_{\text{max}}$ km s <sup>-1</sup> (10)	$L_X^{\text{soft}}$ $10^{40} \text{erg s}^{-1}$ (11)	$L_X^{\text{hard}}$ $10^{40} \text{erg s}^{-1}$ (12)
1	489 ± 85	242 ± 18	2.9 ± 1.8	$17.2 \pm 4.0$	3.1 ± 1.3	$5.51 \pm 0.07$	4.9 ± 1.4	322 ± 25	•••	1.1 <sup>+0.8</sup>	$0.7^{+1.3}_{-0.5}$
2	$344\pm34$		$22.2\pm1.0$		$1.9\pm0.6$	$7.89 \pm 0.09$	$9.0 \pm 2.1$	$296\pm16$	$128 \pm 6$	$2.8_{-0.8}^{+0.9}$	$3.0^{+1.6}_{-1.2}$
3	$437\pm1$	$499 \pm 2$	$2.8 \pm 2.0$	$17.1 \pm 4.0$	$1.7\pm0.5$	$5.49 \pm 0.07$	$5.1\pm1.1$	$291\pm15$		$1.6^{+0.8}_{-0.6}$	$7.6^{+5.9}_{-4.8}$
4	$155\pm3$		$37.8 \pm 0.8$	•••		$1.46\pm0.03$		$277\pm13$			
5	$189 \pm 2$		$31.1\pm0.8$	•••	•••	$1.75 \pm 0.03$	•••	$274\pm15$	•••	•••	

Note. FWHMs and  $EW(H\alpha)$  for the blue and red components only for J102700.40+174900.8 and J102700.38+174902.6.

On the other hand, from the spatially resolved kinematic analysis of Sections 4.1 and 4.2, we show how the ionized extended emission from J102700.55+174900.2 (region 2) partly propagates within the apertures of regions 1 and 3. We can summarize these effects as follows. (a) Parts of the ionized extended emission of J102700.38+174902.6 and J102700.55+174900.2 are collected within aperture 1 (J102700.40+174900.8). (b) Part of the light from the ionized extended emission of J102700.55+174900.2 is collected within aperture 3 (J102700.38+174902.6). (c) The velocity shift from the extended emission of J102700.38+174902.6 is  $\approx\!-150\,\mathrm{km\,s^{-1}}$  at the boundaries of aperture 1. (d) The velocity shift from the extended emission of J102700.55+174900.2 is  $\approx\!40\,\mathrm{km\,s^{-1}}$  at the boundaries of aperture 1, and is  $\approx\!-150\,\mathrm{km\,s^{-1}}$  at the boundaries of aperture 3.

Therefore, the predicted velocity shifts from the spatially resolved kinematic maps are compatible with the velocity shifts of the blue and red components of the integrated spectra of J102700.40+174900.8 and J102700.38+174902.6. This support the hypothesis that the DPAGNs observed in J102700.40+174900.8 and J102700.38+174902.6 are due to the extended emission of J102700.55+174900.2 into apertures 1 and 3 (the red component), and a due to the extended emission of J102700.38+174902.6 into aperture 1 (the blue component).

To explore this point, we measure the positions on the WHAN diagram of the decoupled blue/red components of J102700.40 +174900.8 and J102700.38+174902.6; see Table 7. We measure a  $\log[N\,\textsc{ii}]/\textsc{H}\alpha$  line ratio for the J102700.40+174900.8 red component of  $-0.16\pm0.15,$  with a blue component of  $0.01\pm0.1.$  For J102700.38+174902.6, we get a value of  $0.03\pm0.15$  for the red component and  $0.11\pm0.1$  for the blue component (see Table 7). However, to estimate the EW(H\$\alpha\$), we cannot directly measure the continuum flux for J102700.40+174900.8 and J102700.38+174902.6, because it is not possible to deblend the exact contribution of the continuum flux for each component.

To turn around this problem, we assume that the light fraction of an emission line that is extended within a given aperture is the same as the light fraction of the continuum flux that extends to the same aperture. Therefore, we use the total H $\alpha$  flux of J102700.55+174900.2 and the H $\alpha$  flux of the red component of J102700.38+174902.6 to rescale the J102700.55+174900.2 (aperture 2) continuum flux to estimate the continuum flux of the red component of J102700.38+174902.6 (aperture 3):

$$Cont_{3,R} = Cont_2 \frac{F(H\alpha_{3,R})}{F(H\alpha_2)}.$$
 (6)

The continuum flux associated with the blue component of J102700.38+174902.6 is  $Cont_{3,B} = Cont_3 - Cont_{3,R}$ . With this approximation, we estimate the continuum flux associated with the blue and red components within aperture 3 (J102700.38 +174902.6). The red (blue) component of the continuum flux has a value of  $1.0 \pm 2.0 \times 10^{-16}$  erg s<sup>-1</sup> cm<sup>-2</sup>  $(9.4 \pm 2.0 \times 10^{-16} \text{ erg s}^{-1} \text{ cm}^{-2})$ . Using the same approximation for aperture 1 (J102700.40+174900.8), we find a value of  $1.5 \pm 2.0 \times 10^{-16}$  erg s<sup>-1</sup> cm<sup>-2</sup> for the red component, and a value of  $5.9 \pm 2.0 \times 10^{-16}$  erg s<sup>-1</sup> cm<sup>-2</sup> for the blue component. With these values, we determine the value of EW(H $\alpha$ ) for each component. For J102700.40+174900.8, we find an EW(H $\alpha$ ) value of 2.9  $\pm$  1.8 Å for the blue component and a value of  $17.2 \pm 4.0 \,\text{Å}$  for the red component. For J102700.38+174902.6, we find a value of  $2.8 \pm 2.0 \text{ Å}$  for the blue component and  $17.1 \pm 4.0 \,\text{Å}$  for the red component. We show all these values in Table 6.

We show the final positions on the WHAN diagram in Figure 9. The positions of the red components of J102700.40 +174900.8 and J102700.38+174902.6 are consistent with a strong-AGN ionization and are consistent with the ionization of J102700.55+174900.2. On the other hand, the blue components' positions on the WHAN are at the division between the weak-AGN and fake-AGN regions. However, after considering the errors, both components are consistent with the ionization of J102700.38+174902.6 and J102700.40+174900.8.

# 4.9. X-Ray Data

We have also analyzed archive data from the Chandra Advanced CCD Imaging Spectrometer 0.5–8 keV X-ray of J102700.40+174900.8. This observation was taken by the Chandra program GO3-14104A (PI: Liu), with the ObsID = 14971. These data were observed on 2013 January 23 and are part of an observational program that studies a set of triple AGN candidates (Liu et al. 2019).

We trim the Chandra X-ray image to fit the FOV of MEGARA and show the counts distribution map in the lower right panel of Figure 8. The X-ray compact emission is astrometrically coincident with the optical positions of J102700.55+174900.2 and J102700.38+174902.6. On the locus of J102700.40+174900.8, we observe that there are too few counts, so practically this nucleus does not show X-ray emission, supporting the results obtained with the WHAN diagram. Therefore, it is an object without evidence of AGN activity in these bands, in agreement with recent studies done by Hou et al. (2020) and Foord et al. (2021a, 2021b). On the

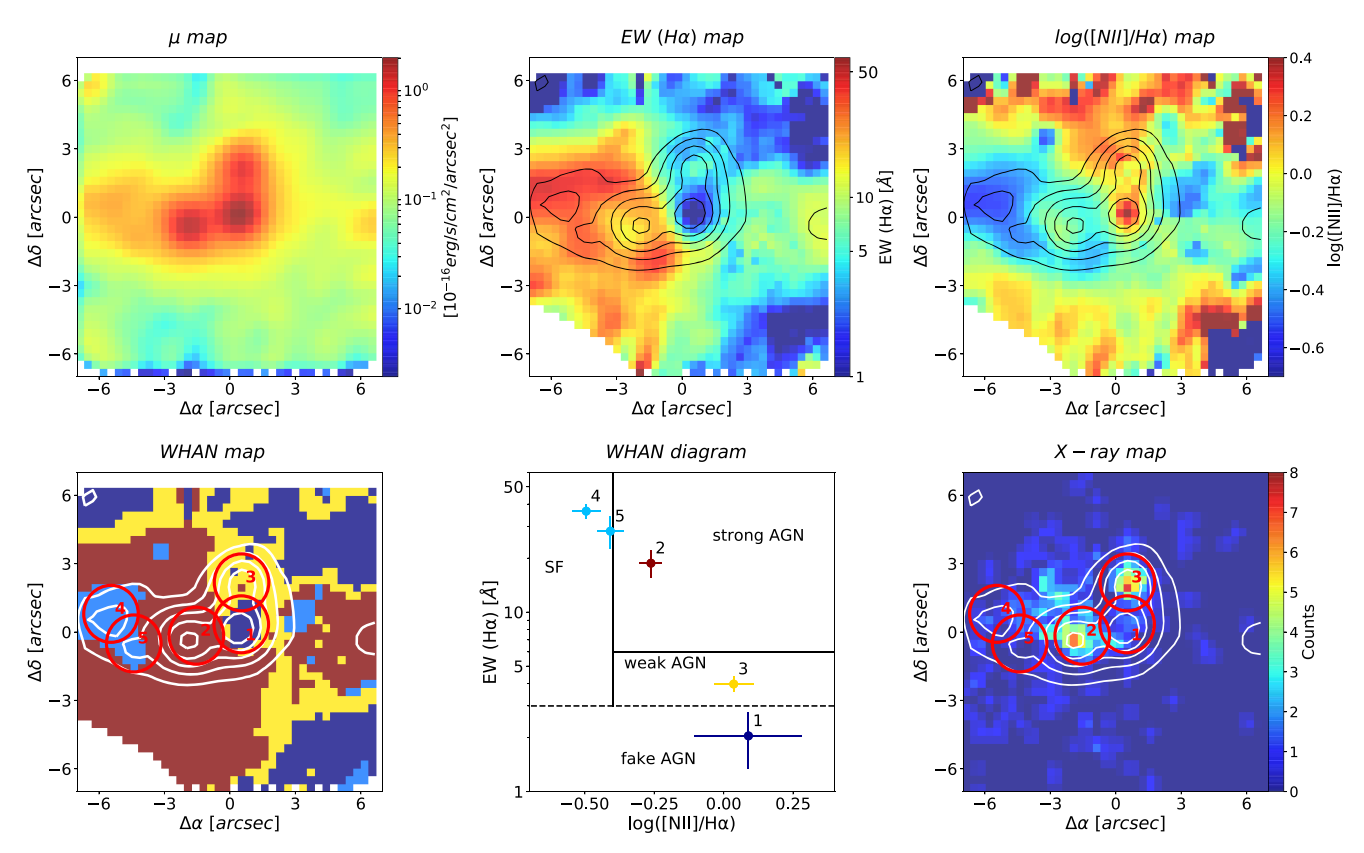


**Figure 8.** Spatially resolved emission line analysis and X-ray map of J102700.40+174900.8. Upper left panel: continuum surface brightness ( $\mu$ ) map of the MEGARA FOV between the rest-frame wavelength range of 6630 Å-6670 Å. Upper central panel: Hα equivalent width map within the MEGARA FOV; the solid black contours represent the continuum  $\mu$  map for reference. Upper right panel: resolved map of the logarithmic line ratio of [N II]/Hα; the solid black contours represent the continuum  $\mu$  map for reference. Lower left panel: spatially resolved WHAN diagram within the MEGARA FOV. The light blue color zones represent the SF emission. The dark blue color represents the fake-AGN emission zones. The yellow color zones represent the weak-AGN emission. The red color zones represent the strong-AGN emission. The white contours represent the continuum  $\mu$  map for reference and the red circles represent the five regions defined in this study. Lower central panel: the WHAN diagram obtained for the five regions; the color code is the same as shown in the lower left panel. Lower right panel: X-ray emission within the MEGARA FOV from Chandra 0.5–8 keV in counts. The red circles represent the five regions. The white contours represent the continuum  $\mu$  map for reference. It is clear that the X-ray emission has very low counts in region 1, i.e., J102700.40+174900.8. J102700.55+174900.2 shows extended X-ray emission toward the north, with a size of  $\sim$ 3.82 kpc.

Table 7
Measured Values of the Blue and Red Components from the Emission Line
Profile Modeling within Regions 1 and 3

	Region 1	Region 3
$H\alpha_R$ Flux	$26 \pm 4$	17 ± 1
$H\alpha_B$ Flux	$17 \pm 4$	$27\pm2$
$\log [N II]/H\alpha_R$	$-0.16 \pm 0.15$	$0.03 \pm 0.15$
$\log [N II]/H\alpha_B$	$0.01 \pm 0.10$	$0.11 \pm 0.10$
$\langle \Delta   V_R \rangle$	$40 \pm 10$	$-150 \pm 10$
$\langle \Delta   V_B \rangle$	$-150\pm10$	$-500 \pm 10$

Note. The line fluxes are in  $10^{-16}$  erg s $^{-1}$  cm $^{-2}$ . The blue and red  $\langle \Delta V \rangle$  are in km s $^{-1}$ .

other hand, J102700.55+174900.2 and J102700.38+174902.6 do show X-ray emission. Furthermore, J102700.55+174900.2 has a clearly extended emission that coincides with part of the extended emission observed toward the NE in EW(H $\alpha$ ).

In order to estimate the X-ray fluxes, we have used the official Chandra analysis tool CIAO<sup>14</sup> to obtain the calibrated

soft (0.5–2 keV) and hard (2–8 keV) luminosities within the 2".5 apertures defined in this study.

We use the tool SRCFLUX<sup>15</sup> from the CIAO package. With SRCFLUX, we estimate the soft and hard X-ray net counts and fluxes from the Chandra X-ray observations. After the net counts extraction, we use a power-law model<sup>16</sup> to estimate the total flux. In addition, SRCFLUX uses a Bayesian computation to estimate the confidence intervals and errors from the extracted fluxes and counts. For the soft X-rays, we get  $13 \pm 3$  ( $F_{\text{soft}} = 1.1^{+0.7}_{-0.6}$ ),  $31 \pm 6$  ( $F_{\text{soft}} = 2.6^{+0.9}_{-0.7}$ ), and  $17 \pm 4$  ( $F_{\text{soft}} = 1.5^{+0.7}_{-0.6}$ ) counts (fluxes  $10^{-15}$  erg s<sup>-1</sup> cm<sup>2</sup>) for regions 1, 2, and 3, respectively. In the same way, we obtain  $2 \pm 1$  ( $F_{\text{hard}} = 0.6^{+1.2}_{-0.5}$ ),  $9 \pm 3$  ( $F_{\text{hard}} = 2.8^{+1.5}_{-1.1}$ ), and  $23 \pm 5$  ( $F_{\text{hard}} = 7.1^{+5.6}_{-4.5}$ ) counts (fluxes  $10^{-15}$  erg s<sup>-1</sup> cm<sup>2</sup>) for the hard X-rays for regions 1, 2, and 3. The background contribution is almost negligible, with  $\approx 0.08$  counts for the soft X-rays and  $\approx 0.2$  counts for the hard X-rays. Finally, the soft and hard X-ray luminosities are shown in Table 6 by using a luminosity distance with z = 0.066.

<sup>14</sup> Chandra Interactive Analysis of Observations: https://cxc.cfa.harvard.edu/ciao/.

https://cxc.cfa.harvard.edu/ciao/ahelp/srcflux.html

<sup>16</sup> https://cxc.cfa.harvard.edu/sherpa/ahelp/xspowerlaw.html

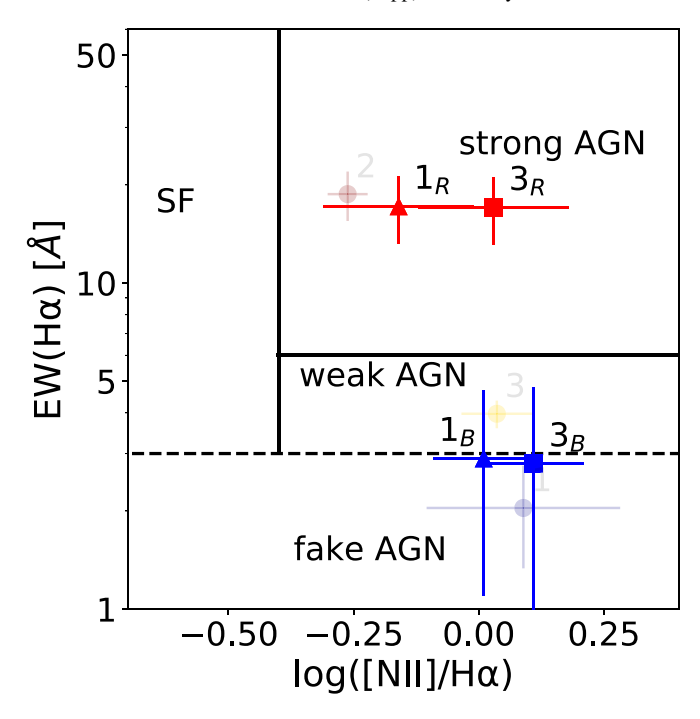


**Figure 9.** WHAN diagram for the deblended blue and red components of the total spectra within regions 1 (triangles) and 3 (squares). The blue color represents the blue components, and the red color represents the red components. The positions of the averaged resolved values within apertures 1, 2, and 3 are overplotted with lighter colors, following the color code of Figure 8.

#### 5. Discussion

Multiple AGN systems are expected to be found in the framework of the hierarchical model of galaxy formation. Since the source J102700.40+174900.8 is among the few triple AGN candidate systems known to date, GTC/MEGARA observations are ideal for studying the nature and kinematics at kiloparsec scales of these nuclei that are associated with this field. The spatially resolved data cube image obtained with MEGARA allows the establishment of the extension of the ionized emission gas and the kinematical properties of each nucleus. The WHAN diagram was chosen to provide the classification of the nuclei, since the blue parts of the MEGARA spectra could not be used in this analysis. This was due to the high obscuration and low S/N obtained in these parts of the spectra, so the BPT diagnostic diagrams could not be obtained.

Our stellar mass estimation of J102700.40+174900.8 was compared with the ones obtained by L11 and (Chang et al. 2015; hereafter, C15). In our case, we have considered the stellar mass correction from a Chabrier/Kroupa IMF to a Salpeter IMF. So, we find a stellar mass value of  $5.51 \times 10^{10} M_{\odot}$ . On the other hand, L11 obtained a stellar mass of  $2.6 \times 10^{11} M_{\odot}$ , while C15 obtained a value of  $1.7 \times 10^{11} M_{\odot}$ . The smaller value obtained by us could be due to differences in the total aperture size, and in the way that PYPIPE3D calculates the internal dust extinction. For instance, if we calculate the total stellar mass within the SDSS fiber aperture, we find a total value of  $8.6 \pm 0.1 \times 10^{10} M_{\odot}$  for J102700.40+174900.8. In addition, the stellar masses

estimated from spectral energy distribution (SED) fitting, which use optical spectra (in the case of L11) or panchromatic SED fitting (C15), are subject to large systematic uncertainties, due to a complex mix of dust extinction, stellar libraries, inclination, etc. (see Ibarra-Medel et al. 2019).

The WHAN diagram shows that J102700.40+174900.8, previously identified as a LINER by L11, is instead an RG that does not have activity produced by either an AGN or SF. Also, we find that J102700.40+174900.8 is a DPAGN, based on our analysis of the 1D SDSS spectrum shown in Figure 3. However, MEGARA data analysis clearly shows that the origin of the double-peaked narrow emission lines in J102700.40+174900.8 is the extended narrow emission coming from J102700.55+174900.2, and also the weak-AGN emission from J102700.38+174902.6 (see the upper right panel of Figure 6). Therefore, we have a case where a DPAGN classification leads us to misclassify an RG as a DPAGN. Meanwhile, the DPAGN observed within region 3 (J102700.38 +174902.6) is due to the ionized extended emission of J102700.55+174900.2, plus its intrinsic ionized emission, so in this case J102700.38+174902.6 is a DPAGN.

The spatially resolved WHAN diagram shows that the source of the ionization emission in J102700.40+174900.8 is hot low-mass evolved stars (Stasińska et al. 2004; Cid Fernandes et al. 2011). This is also supported by the high value of log [N II]/H $\alpha$  (0.2 dex) and the low value of EW(H $\alpha$ ) found in the WHAN diagram for J102700.40+174900.8. Therefore, it is easy to misclassify an RG as a LINER-like object using only the BPT diagrams and as a DPAGN using longslit spectroscopy.

This result is also confirmed by revisiting the Chandra X-ray data of J102700.40+174900.8. The X-ray counts map shows basically no emission being produced by this RG. The HST optical–UV and NIR images show that it has an elliptical morphology, typical of RGs. So, our analysis suggests that J102700.40+174900.8 is not an AGN. Therefore, these results rule out the triple-AGN nature of the triplet of galaxies, at least in the optical and X-ray bands.

In the WHAN diagram, J102700.55+174900.2 appears as a strong AGN. Due to its redshift, we classify it as a Seyfert 2 (Sy2) galaxy. The Sy2 classification is also supported by the results obtained from the MCMC modeling of the spaxels of the data cube. The model shows that no broad emission line components appear to be present in either of the three nuclei within the  $1\sigma$  confidence level. The isovelocity map shows that J102700.55+174900.2 has a rotating gaseous disk, and the WHAN diagram confirms the presence of a kiloparsec-scale extended  $H\alpha$  emission region associated with this Sy2. This galaxy was previously classified as a composite AGN by L11.

The X-ray data for J102700.55+174900.2 show emission at 0.5–8 keV, and also extended emission with a size of  $\sim$ 3.8 kpc that coincides with the NE extended emission observed in the WHAN diagram. HST images reveal that J102700.55+174900.2 shows signs of interaction, with a disrupted ring that shows emission from SF regions located at regions 4 and 5, as shown in the WHAN diagrams. We find that the LOS velocity difference between J102700.55+174900.2 and J102700.40+174900.8 is only  $\approx$ 4 km s<sup>-1</sup>.

In the case of J102700.38+174902.6, it was found to be a weak AGN, in this case, a LINER2 (e.g., Terashima et al. 2000). The HST NIR and optical—UV images show that this object has a spiral morphology, although the HST images show it with wider opened spiral arms produced by the interaction

<sup>&</sup>lt;sup>17</sup> We use scale factors of 0.21 dex and 0.20 dex to go from a Chabrier/ Kroupa to a Salpeter IMF (Madau & Dickinson 2014).

with J102700.55+174900.2 and J102700.40+174900.8. In fact, with our data, we find that J102700.38+174902.6 is moving with respect to J102700.55+174900.2 and J102700.40 +174900.8, with a velocity of  $\approx$  -500 km s<sup>-1</sup>.

#### 6. Conclusions

The kinematical analysis presented in this work shows that the northern nucleus is moving with respect to the southeastern nucleus with a speed of ~-500 km s<sup>-1</sup>. This large velocity suggests that both AGNs are in a late minor merger phase. We have also found that both are obscured objects, in agreement with the L11 results. If the northern nucleus passes near the center of the disk of the southeastern nucleus, after n passings, it can produce a collisional ring with knots, a morphology that is observed in the NIR and optical–UV HST images, and is also in agreement with the results from numerical simulations (e.g., Theys & Spiegel 1977; Renaud et al. 2018). Since the northern nucleus is the less massive companion galaxy, and interacts with the southeastern nucleus via a head-on collision, the latter object is predicted to end up with lenticular morphology as a consequence of this kind of interaction (Bekki 1998; Giri et al. 2023).

Finally, we have shown that the former triple AGN candidate in J102700.40+174900.8 is instead a DAGN system, where the central nucleus of the system is not an AGN. The three nuclei are characterized by the spatially resolved WHAN diagram, the center nucleus being an RG, the northern nucleus a LINER2, and the southeastern nucleus a Sy2 galaxy. So, the DAGN system consists of a Sy2-LINER2 pair, with a projected separation of 3.98 kpc. This DAGN system is confirmed in the optical and X-ray data analyzed in this work.

## Acknowledgments

We thank the anonymous referee for their valuable comments and suggestions. E.B., I.C.G., and J.M.R.E. acknowledge support from DGAPA-UNAM grant IN113320. I.C.G., E.B., H.I.B., C.A.N., and J.M.R.E. acknowledge support from DGAPA-UNAM grant IN119123. C.A.N. is grateful for support from DGAPA-UNAM grant IN111422 and CONACyT project Paradigmas y Controversias de la Ciencia 2022-320020. H.I.M. acknowledges support from the Instituto Politécnico Nacional (México). J.M.R.E. acknowledges the Spanish State Research Agency under grant number AYA2017-84061-P. J.M.R.E. also acknowledges the Canarian Government under the project PROID2021010077, and is indebted to the Severo Ochoa Programme at the IAC. X.L. acknowledges support from NSF grant AST-2108162. Based on observations made with the Gran Telescopio Canarias (GTC), installed at the Spanish Observatorio del Roque de los Muchachos of the Instituto de Astrofísica de Canarias, on the island of La Palma. This work is based on data obtained with the MEGARA instrument, funded by European Regional Development Funds (ERDF), through Programa Operativo Canarias FEDER 2014–2020. We acknowledge the support given by the GTC-MEGARA staff, in particular Antonio Cabrera. This work is partly based on observations made with the NASA/ESA Hubble Space Telescope, obtained from the data archive at the Space Telescope Science Institute. STScI is operated by the Association of Universities for Research in Astronomy, Inc., under NASA contract NAS 5-26555. Funding for the Sloan Digital Sky Survey V has been provided by the Alfred P. Sloan Foundation, the Heising-Simons Foundation,

the National Science Foundation, and the Participating Institutions. S.D.S.S. acknowledges support and resources from the Center for High-Performance Computing at the University of Utah. The SDSS website is www.sdss.org. Support for Chandra program number 14700279 was provided by NASA through Chandra Award Number GO3-14104X issued by the Chandra X-ray Observatory Center, which is operated by the Smithsonian Astrophysical Observatory for and on behalf of NASA under contract NAS 8-03060. This research has made use of the NASA/IPAC Extragalactic Database (NED), which is operated by the Jet Propulsion Laboratory, California Institute of Technology, under contract with the National Aeronautics and Space Administration. E.B. and I.C. G. acknowledge support from Conacyt Grant CF-2023-G-100. Facilities: GTC/(MEGARA-IFU), CXO (ACSIS), HST (WFC3), Sloan Digital Sky Survey Legacy DR7.

Software: MEGARA DRP: https://megaradrp.readthedocs.io/en/stable/, PYPIPE3D (Sánchez et al. 2022), IRAF/specfit (Kriss 1994).

## ORCID iDs

```
Erika Benítez https://orcid.org/0000-0003-1018-2613
Héctor Ibarra-Medel https://orcid.org/0000-0002-9790-6313
Castalia Alenka Negrete https://orcid.org/0000-0002-1656-827X
Irene Cruz-González https://orcid.org/0000-0002-2653-1120
José Miguel Rodríguez-Espinosa https://orcid.org/0000-0002-0674-1470
Xin Liu https://orcid.org/0000-0003-0049-5210
Yue Shen https://orcid.org/0000-0003-1659-7035
```

#### References

```
Abazajian, K. N., Adelman-McCarthy, J. K., Agüeros, M. A., et al. 2009,
   ApJS, 182, 543
Aquino-Ortíz, E., Valenzuela, O., Sánchez, S. F., et al. 2018, MNRAS,
  479, 2133
Baldwin, J. A., Phillips, M. M., & Terlevich, R. 1981, PASP, 93, 5
Barnes, J. E. 2004, MNRAS, 350, 798
Barnes, J. E., & Hernquist, L. 1996, ApJ, 471, 115
Barnes, J. E., & Hernquist, L. E. 1991, ApJL, 370, L65
Bekki, K. 1998, ApJ, 499, 635
Benítez, E., Cruz-González, I., Rodríguez-Espinosa, J. M., et al. 2019,
  MNRAS, 490, 5521
Benítez, E., Jiménez-Bailón, E., Negrete, C. A., et al. 2022, MNRAS,
  516, 5270
Bennett, C. L., Larson, D., Weiland, J. L., & Hinshaw, G. 2014, ApJ, 794, 135
Bertola, F., Bettoni, D., Danziger, J., et al. 1991, ApJ, 373, 369
Blecha, L., Loeb, A., & Narayan, R. 2013, MNRAS, 429, 2594
Blecha, L., Snyder, G. F., Satyapal, S., & Ellison, S. L. 2018, MNRAS,
  478, 3056
Blumenthal, K. A., & Barnes, J. E. 2018, MNRAS, 479, 3952
Capelo, P. R., Dotti, M., Volonteri, M., et al. 2017, MNRAS, 469, 4437
Cardelli, J. A., Clayton, G. C., & Mathis, J. S. 1989, ApJ, 345, 245
Carrasco, E., Gil de Paz, A., Gallego, J., et al. 2018, Proc. SPIE, 10702,
Chang, Y.-Y., van der Wel, A., da Cunha, E., & Rix, H.-W. 2015, ApJS, 219, 8
Chien, L. H., & Barnes, J. E. 2010, MNRAS, 407, 43
Cid Fernandes, R., Pérez, E., García Benito, R., et al. 2013, A&A, 557, A86
Cid Fernandes, R., Stasińska, G., Mateus, A., & Vale Asari, N. 2011, MNRAS,
  413, 1687
De Rosa, A., Vignali, C., Bogdanović, T., et al. 2019, NewAR, 86, 101525
Di Matteo, T., Colberg, J., Springel, V., Hernquist, L., & Sijacki, D. 2008, ApJ,
  676. 33
Di Matteo, T., Springel, V., & Hernquist, L. 2005, Natur, 433, 604
```

Ferrarese, L., & Merritt, D. 2000, ApJL, 539, L9

```
Filippenko, A. V. 1982, PASP, 94, 715
Fitzpatrick, E. L. 1999, PASP, 111, 63
Foord, A., Gültekin, K., Runnoe, J. C., & Koss, M. J. 2021a, ApJ, 907, 71
Foord, A., Gültekin, K., Runnoe, J. C., & Koss, M. J. 2021b, ApJ, 907, 72
Foreman-Mackey, D., Hogg, D. W., Lang, D., & Goodman, J. 2013, PASP,
Ge, J.-Q., Hu, C., Wang, J.-M., Bai, J.-M., & Zhang, S. 2012, ApJS, 201, 31
Gebhardt, K., Bender, R., Bower, G., et al. 2000, ApJL, 539, L13
Giri, G., Barway, S., & Raychaudhury, S. 2023, MNRAS, 520, 5870
Hamuy, M., Walker, A. R., Suntzeff, N. B., et al. 1992, PASP, 104, 533
Heckman, T. M. 1980, A&A, 87, 152
Hopkins, P. F., Cox, T. J., Hernquist, L., et al. 2013, MNRAS, 430, 1901
Hopkins, P. F., Hernquist, L., Cox, T. J., et al. 2006, ApJS, 163, 1
Hopkins, P. F., Hernquist, L., Cox, T. J., & Kereš, D. 2008, ApJS, 175, 356
Hou, M., Li, Z., & Liu, X. 2020, ApJ, 900, 79
Ibarra-Medel, H. 2022, MNRAS, 515, 6032
Ibarra-Medel, H., Avila-Reese, V., Lacerna, I., et al. 2022, MNRAS, 510, 5676
Ibarra-Medel, H. J., Avila-Reese, V., Sánchez, S. F., González-Samaniego, A., &
   Rodríguez-Puebla, A. 2019, MNRAS, 483, 4525
Kim, D. C., Yoon, I., Evans, A. S., et al. 2020, ApJ, 904, 23
Kormendy, J., & Richstone, D. 1995, ARA&A, 33, 581
Kriss, G. 1994, in ASP Conf. Ser. 61, Astronomical Data Analysis Software
   and Systems III, ed. D. R. Crabtree, R. J. Hanisch, & J. Barnes (San
   Francisco, CA: ASP), 437
Lacerda, E. A. D., Sánchez, S. F., Mejía-Narváez, A., et al. 2022, NewA, 97,
Law, D. R., Cherinka, B., Yan, R., et al. 2016, AJ, 152, 83
Liu, X., Hou, M., Li, Z., et al. 2019, ApJ, 887, 90
Liu, X., Shen, Y., & Strauss, M. A. 2011, ApJL, 736, L7
Liu, X., Shen, Y., Strauss, M. A., & Greene, J. E. 2010, ApJ, 708, 427
Madau, P., & Dickinson, M. 2014, ARA&A, 52, 415
Magorrian, J., Tremaine, S., Richstone, D., et al. 1998, AJ, 115, 2285
McConnell, N. J., & Ma, C.-P. 2013, ApJ, 764, 184
Moffat, A. F. J. 1969, A&A, 3, 455
```

```
Pfeifle, R. W., Satyapal, S., Manzano-King, C., et al. 2019, ApJ, 883, 167
Renaud, F., Athanassoula, E., Amram, P., et al. 2018, MNRAS, 473, 585
Salpeter, E. E. 1955, ApJ, 121, 161
Sánchez, S. F. 2020, ARA&A, 58, 99
Sánchez, S. F., Barrera-Ballesteros, J. K., Lacerda, E., et al. 2022, ApJS,
  262, 36
Sánchez, S. F., Kennicutt, R. C., Gil de Paz, A., et al. 2012, A&A, 538, A8
Sánchez, S. F., Pérez, E., Sánchez-Blázquez, P., et al. 2016a, RMxAA, 52, 21
Sánchez, S. F., Pérez, E., Sánchez-Blázquez, P., et al. 2016b, RMxAA, 52,
Schlafly, E. F., & Finkbeiner, D. P. 2011, ApJ, 737, 103
Smart, W. M. 1931, Text-book on Spherical Astronomy (Cambridge:
  Cambridge Univ. Press)
Smith, K. L., Shields, G. A., Bonning, E. W., et al. 2010, ApJ, 716, 866
Springel, V., Di Matteo, T., & Hernquist, L. 2005, ApJL, 620, L79
Stasińska, G., Mateus, A. J., Sodré, L. J., & Szczerba, R. 2004, A&A,
  420, 475
Terashima, Y., Ho, L. C., Ptak, A. F., et al. 2000, ApJ, 533, 729
Theys, J. C., & Spiegel, E. A. 1977, ApJ, 212, 616
Tremaine, S., Gebhardt, K., Bender, R., et al. 2002, ApJ, 574, 740
Trujillo, I., Aguerri, J. A. L., Cepa, J., & Gutiérrez, C. M. 2001, MNRAS,
  328, 977
Van Wassenhove, S., Volonteri, M., Mayer, L., et al. 2012, ApJL, 748, L7
Vanden Berk, D. E., Richards, G. T., Bauer, A., et al. 2001, AJ, 122, 549
Veilleux, S., & Osterbrock, D. E. 1987, ApJS, 63, 295
Wang, J.-M., Chen, Y.-M., Hu, C., et al. 2009, ApJL, 705, L76
Weiner, B. J., Willmer, C. N. A., Faber, S. M., et al. 2006, ApJ, 653, 1027
White, S. D. M., & Frenk, C. S. 1991, ApJ, 379, 52
White, S. D. M., & Rees, M. J. 1978, MNRAS, 183, 341
Wright, E. L. 2006, PASP, 118, 1711
Yadav, J., Das, M., Barway, S., & Combes, F. 2021, A&A, 651, L9
York, D. G., Adelman, J., Anderson, J. E. J., et al. 2000, AJ, 120, 1579
Zwicky, F. 1937, ApJ, 86, 217
```

Oke, J. B. 1990, AJ, 99, 1621